RESEARCH PAPER

Bubble Collapse Inside Rigid Ellipsoid Using Boundary Integral Method in Axisymmetric Configuration.

Hawchin Jabar Ahmed[1], Kawa M.A. Manmi [2]
1Department of Mathematics, Faculty of Science, Soran University, Soran -Erbil, Kurdistan Region, Iraq.
2Department of Mathematics, College of Science, Salahaddin University-Erbil, Kurdistan Region, Iraq.

A B S T R A C T:

A high-speed liquid jet forms toward the closest side of the boundary when a bubble collapses near a solid boundary. This is associated with important applications in cleaning microdevices, chemical reactions (sonochemistry) and biomedical ultrasound. In this work, bubble expansion, collapse and jet formation inside a rigid ellipsoid boundary have been investigated using the boundary integral method (BIM) in an axisymmetric configuration. We assume that the fluid flows satisfy the potential flow theory and the bubble is initially spherical with high gas pressure. Then the bubble growth and subsequently collapse non-spherically. Eventually high-speed liquid jet forms toward the nearby rigid boundary(s). The numerical results validated with the Rayleigh-Plesset equation for a spherical bubble oscillation at infinite fluid for several cycles as well as self-validating with considering image and without image method for using Green's function in the BIM. Then, three different vertical standoff distances from the center of the bubble to the boundary of the ellipsoid have been considered to investigate the bubble motion behavior including jet velocity, jet width, Kelvin impulse and centroid movement. It was concluded that the standoff distances and ellipsoid radius were significant factors on the bubble behaviour.

1. INTRODUCTION:

In many manmade and natural systems, cavitation phenomenon is occurred which is defined as the formation, growth and collapse of bubbles in a flowing liquid, in a region where the pressure of the liquid suddenly drops below a threshold value (Castro, 2019; Aziz, 2019; Mahmud, 2020). As the fluid pressure drops below to vapor pressure, cavities begin to develop. Subsequently, the pressure is further reduced, causing vapor bubbles to expand simultaneously with the flow. The sudden expansion and collapse of these bubbles produce extreme pressure that hit the near surfaces and cause damage (Mahmud, 2020; Rayleigh, 1917; Nadir and MANMI, 2020) and erosion. On other hand, cavitation has increasingly found many beneficial applications in science and eng-ineering including medical science, mechanical engineering, chemical engineering, ocean engi-neering, shipbuilding engineering, nanomaterial engineering, environmental engineering, nuclear engineering, and biomedical engineering (Manmi, 2015; Aziz, 2019; Mahmud, 2020; Liu, 2018).

Usually, bubble tends to oscillate spherically due to surface tension, however, when it is nearby structure, it become non-spherical and eventually high speed liquid jet forms toward the structure which is believed it has main role for surface damaging or removed particles of the surface. The oscillations of a single bubble have been widely studied experimentally and mathematically in the literature to understand the mechanism of liquid jet formation near simple or/and complex boun-daries or structures. For example, experimental attempts; such as (Lindau and Lauterborn, 2003) investigated jet formation near horizontal wall, (Cui et al., 2021; Cui et al., 2022) considered bubble dynamics near rigid incomplete plate, behavior of a laser-induced cavitation bubble near

Ahmed. H. *and*. Manmi .K . /ZJPAS: 2023, 35 (2): 63-77

64

two perpendicular rigid walls by (Brujan et al., 2018), (Su et al., 2022) studied the complex dynamics of underwater explosion bubble between two parallel plates, and (Fourar and Bories, 1995) considered of air-water two-phase flow through narrow channel.

Mathematical modeling is another alternative approach to study the phenomena analytically and numerically. Rayleigh-Plesset equation (RPE) is the first and foremost mathematical model for describing nonlinear response of a gas bubble motion, which is a nonlinear ordinary differential equation based on mass and momentum conservation under the assumption of spherical symmetry (Leighton, 2007; Lin et al., 2002), in an infinite incompressible, liquid medium with no gravity, surface tension, viscosity, heat or mass transfer (Plesset and Prosperetti, 1977; Rayleigh, 1917; Plesset, 1954; Sarkar, 2019; Nadir and MANMI, 2020).

In 1956, Keller and Kolodner (Keller and Kolodner, 1956) extended Rayleigh-Plesset formula for the Keller-Miksis equation (KME) of the oscillations of a spherical bubble in a compressible liquid (Lauterborn and Kurz, 2010). The major difference between the KME and RPE is that the KMF does not assume the liquid to be incomeepressible (Keller and Miksis, 1980). Several extension of RPE and KME in different scenarios have been proposed for instance, bubble oscillation in an elastic solid (Wang, 2017; Doinikov and Marmottant, 2018; Doinikov et al., 2018; Doinikov et al., 2019, Wang et al., 2018), modified the conventional Rayleigh–Plesset (Soliman et al., 2010; Klaseboer and Khoo, 2006; Alehossein and Qin, 2007; Tey et al., 2020).

On the other hand, numerical attempts such as (Zhang et al., 2013) were investigated bubble dynamics between two boundaries, experimental and numerical model of bubble oscillation between rigid walls by (Ogasawara et al., 2015), experimental and numerical investigation of bubble oscillation in a narrow tube (Ni et al., 2012), bubble oscillation inside a vertical rigid cylinder studied by (Mehran et al., 2010), bubble oscillation between two parallel heated walls (Liu et al., 2014), and bubble dynamics near a plate with a circular aperture in a vertical cylinder (Dawoodian et al., 2015).

The boundary integral method (BIM) is an elegant technique which reduces the dimensionality of many numerical problems by one. This is accomplished by transforming the differential equations integrally, which moves the evaluation from the computing domain's volume to its surface (Manmi 2015; Klaseboer et al., 2009; Blake et al., 1986; Blake et al., 1987; Chahine and Perdue, 1990). Acoustic bubble dynamics were simulated using an axisymmetric BIM model for a bubble in an infinite liquid and near a boundary subject to ultrasound propagating in the direction perpendicular to the boundary (Manmi, 2015). The boundary element approach is essentially a method for solving partial differential equations (PDEs) and can only be used when the physical issue can be represented as such, much like the more well-known finite element method (FEM) and finite difference method (FDM). The boundary element approach is a numerical method, like the other methods described. As a result, the numerical analysis community places a high priority on research into this technique (Aziz, 2019; Manmi, 2015).

Recently, bubble oscillations inside a spherical liquid filled cavity surrounded by an elastic spherical medium have been attention by many researchers including (Wang, 2017; Wang et al., 2018; Doinikov et al., 2019; Zhang et al., 2022). The phenomena motivated by application, in biology (Jensen et al., 2016), dynamics of porous media (Vincent et al., 2014), geology (Marti et al., 2012) and sap cavitation occurs when the tree's pumping system is operating under a negative pressure less than the threshold pressure (Cochard, 2006). The research attention was focused on the boundary, which is completely spherical, and the bubble located at the center of the sphere. Further, their studies were theoretical for linear and nonlinear bubble oscillations. However, our numerical model is for bubble dynamics inside a rigid ellipsoid with a center not located at the origin. We used BIM to investigate bubble collapse inside a rigid ellipsoid at different initial inceptions. When bubble growth near the rigid boundary subsequently collapse no-spherical and in most cases, high liquid jet forms toward the rigid boundary. The characteristics of the liquid jet depend on the type and shape of the rigid boundary as well as the distance from the bubble center to the rigid boundary. Eventually, when the jet develops the bubble becomes toroidal and high liquid jet might hit the surface of the boundary. It could damage the surface, which might lead to

Ahmed. H. *and*. Manmi .K . /ZJPAS: 2023, 35 (2): 63-77

65

destructor removing the particles from the surface of the boundary.

The rest of the paper is organized as follows: In Section 2, mathematical and physical models are presented. Section 3 describes kinematic and dynamic boundary conditions. Dimensionless variables in Section 4. Section 5 numerical model. Validation of the numerical model in Section 6. In Section 7, results are presented and discussed and finally, in Section 8, conclusions are given.

2. Mathematical and Physical Model

Consider a bubble oscillation in a rigid ellipsoid filled with liquid. Suppose that the boundary of the liquid domain D is denoted by S, $S = S_b + S_r$, where S_b and S_r (see red lines in Figure 1) are the bubble surface and rigid ellipsoid boundaries respectively. The schematic of the model in (r, z) coordinates systems is illustrated in Figure 1,

when the axis of symmetry is along z-axis. We assume that initially a spherical bubble with center at $(0, z)$ and radius R_0 oscillates inside a rigid ellipsoid with center at the origin, major radius R_{cM} and minor radius R_{cm}. The distance between the center of the initial bubble and the rigid boundary is denoted by h_s. Assume that the fluid is inviscid it means that the fluids with zero viscosity, also the fluid is incompressible by continuity equation $\nabla \cdot \mathbf{u} = 0$, where ∇ is gradient and $\mathbf{u}$ is the fluid velocity, and the fluid flow is irrotational ($\nabla \times \mathbf{u} = \mathbf{0}$). So, the flow is potential where the fluid velocity $\mathbf{u}$ defined as the gradient of the velocity potential φ, $\mathbf{u} = \nabla\varphi$ which satisfies the Laplace's equation $\nabla^2\varphi = 0$. Using the second Green identity, the velocity potential thus transformed into the boundary integral equation as follows (Manmi, 2015; Aziz, 2019; Mahmud, 2020; Liu, 2018; Curtiss, 2009),

$$c(\mathbf{p})\varphi(\mathbf{p}) = \int_S \left(\frac{\partial\varphi(\mathbf{q})}{\partial\mathbf{n}} G(\mathbf{p},\mathbf{q}) - \varphi(\mathbf{q}) \frac{\partial G(\mathbf{p},\mathbf{q})}{\partial\mathbf{n}} \right) dS(\mathbf{q}), \tag{1}$$

where $\mathbf{p}$ is the field point and $\mathbf{q}$ is the source point, $c(\mathbf{p})$ is the solid angle at the field vector $\mathbf{p}$ and $\mathbf{n}$ is the outward unit normal to the boundaries S. The solid angle is given by,

$$c(\mathbf{p}) = \begin{cases} 4\pi & if & \mathbf{p} \in D\backslash S \\ 2\pi & if & \mathbf{p} \in S \end{cases}. \tag{2}$$

Hence this Green's function, $G(\mathbf{p},\mathbf{q})$ can be defined as,

$$G(\mathbf{p},\mathbf{q}) = \frac{1}{|\mathbf{p}-\mathbf{q}|}. \tag{3}$$

Using cylindrical coordinates with $\mathbf{q} = (r, \theta, z)$ and $\mathbf{p} = (r_i, \theta_i, z_i)$, the distance between the points $\mathbf{q}$ and $\mathbf{p}$ is given as,

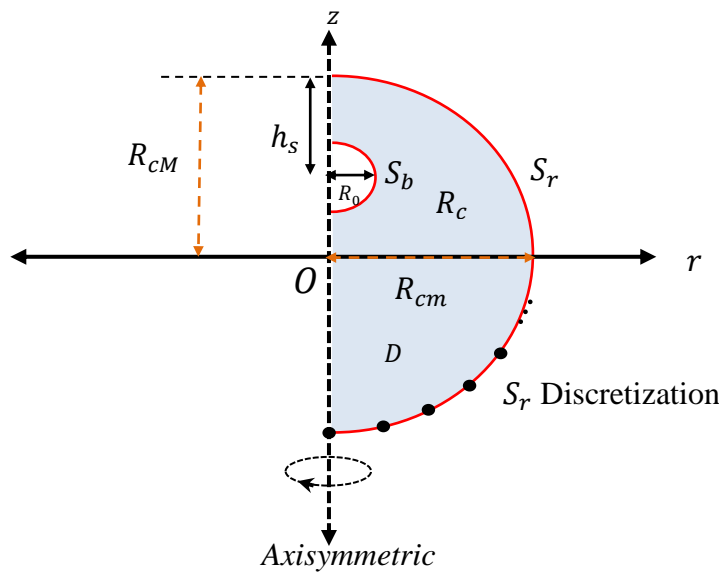$$|\mathbf{p}-\mathbf{q}| = \sqrt{r^2 + r_i^2 - 2rr_i \cos(\theta - \theta_i) + (z - z_i)^2}. \tag{4}$$

Figure 1: Schematic of a bubble dynamics inside rigid ellipsoid filled with the liquid.

3. Kinematic and Dynamic Boundary Conditions

The kinematic boundary conditions on the bubble surface require a liquid particle to remain on the bubble surface, i.e.

$$\frac{d\mathbf{r}}{dt} = \nabla\varphi, \qquad \mathbf{r} \in S_b. \tag{5}$$

On the rigid boundaries,

$$\nabla\varphi \cdot \mathbf{n} = \mathbf{U} \cdot \mathbf{n}, \tag{6}$$

where, $\mathbf{U}$ is a local velocity vector of the rigid surface. For an infinite plane solid wall the $\mathbf{U} = 0$, and condition (6) is met exactly by reflection the flow field and the boundaries in the wall and by removing the wall (Wang and Manmi, 2014; Aziz, 2019),

$$\nabla\varphi \cdot \mathbf{n} = \mathbf{0}. \tag{7}$$

The momentum conservation considering the irrationality and incompressibility provides the Bernoulli's equation is defined as follows (Batchelor, 2000; Cengel and Cimbala, 2014),

$$\frac{\partial\varphi}{\partial t} + \frac{1}{2}|\nabla\varphi|^2 + \frac{p_L}{\rho} + gz = c(t), \tag{8}$$

where, ρ and p_L are density and pressure of the liquid respectively, and $c(t)$ is arbitrary function of t. Far-field boundary conditions are used to determine the value of $c(t)$, we assume that the boundary conditions at infinity are,

$$\mathbf{u} \longrightarrow 0, \tag{9}$$

$$p \longrightarrow p_\infty, \tag{10}$$

use equations (9) and (10) in equation (8), we have $c(t) = \frac{p_\infty}{\rho}$, substituting $c(t)$ in equation (8) we get,

$$\frac{\partial\varphi}{\partial t} + \frac{1}{2}|\nabla\varphi|^2 + \frac{p_L}{\rho} + gz = \frac{p_\infty}{\rho}. \tag{11}$$

The dynamic boundary condition on the bubble surface is obtained from balancing the bubble surface pressure including surface tension effects for an inviscid fluid as follows (Aziz, 2019; Mahmud, 2020),

$$p_L = p_b - 2\sigma r_c, \tag{12}$$

where p_L is the liquid pressure on the bubble surface, p_b is the pressure inside bubble, σ is the surface tension coefficient on the flow domain, and $r_c = \nabla \cdot \mathbf{n}$ is the mean curvature of the bubble surface. Substituting equation (12) into equation (11) we obtain,

$$\rho\frac{\partial\varphi}{\partial t} + \frac{1}{2}\rho|\nabla\varphi|^2 + \rho gz + p_b - 2\sigma(\nabla \cdot \mathbf{n}) = p_\infty. \tag{13}$$

Now substituting the material derivative of φ,

$$\frac{d\varphi}{dt} = \frac{\partial\varphi}{\partial t} + \mathbf{u} \cdot \nabla\varphi, \tag{14}$$

into equation (13) we get,

$$\rho\frac{d\varphi}{dt} = \frac{1}{2}\rho\nabla^2\varphi - \rho gz + 2\sigma(\nabla \cdot \mathbf{n}) + p_\infty - p_b. \tag{15}$$

It is supposed that the pressure inside the bubble p_b is uniform and the bubble contains non-condensable gas and condensable water vapor. The non-condensable gas is supposed to satisfy the polytropic law. The vapor pressure and the gas pressure are considered dilute enough so their pressures can be expressed by Dalton's law for mixtures of ideal gases (Brennen, 2014),

$$p_b = p_c + p_g, \tag{16}$$

where p_c is the condensable vapor pressure and p_g is partial pressure of the gas,

$$p_g = p_0\left(\frac{V_0}{V}\right)^\lambda. \tag{17}$$

Thus, the pressure p_b inside the bubble can be related to the bubble volume V as follows,

$$p_b = p_c + p_0\left(\frac{V_0}{V}\right)^\lambda. \tag{18}$$

Here p_0 denotes the initial gas pressure inside the bubble, V is volume of the bubble and where $\lambda = \frac{c_p}{c_V}$, where c_p is specific heat at constant pressure and c_V is specific heat at constant volume. Using equation (18) into equation (15) we yield,

$$\rho\frac{d\varphi}{dt} = p_\infty - p_c + \frac{1}{2}\rho|\nabla\varphi|^2 - \rho gz + 2\sigma(\nabla \cdot \mathbf{n}) - p_0\left(\frac{V_0}{V}\right)^\lambda. \tag{19}$$

The dynamic boundary condition on the bubble surface can be written as,

$$\frac{d\varphi}{dt} = \frac{p_\infty - p_c}{\rho} + \frac{1}{2}|\nabla\varphi|^2 - gz + 2\frac{\sigma}{\rho}(\nabla \cdot \mathbf{n}) - \frac{p_0}{\rho}\left(\frac{V_0}{V}\right)^\lambda. \tag{20}$$

Ahmed. H. *and*. Manmi .K . /ZJPAS: 2023, 35 (2): 63-77

67

4. Dimensionless Variables

The variables are normalized using the initial radius of the bubble R_m, and $\Delta p = p_\infty - p_c$ as follows (Wang, 2013; Wang and Manmi, 2014; Manmi, 2015),

$$t_* = \frac{t}{R_m}\sqrt{\frac{\Delta p}{\rho}}, \qquad \boldsymbol{r}_* = \frac{\boldsymbol{r}}{R_m}. \tag{21}$$

$$z_* = \frac{z}{R_m}. \tag{22}$$

First, dynamic boundary conditions (20) can written as,

$$\frac{\rho}{\Delta p}\frac{d\varphi}{dt} = 1 + \frac{1}{2}\frac{\rho}{\Delta p}|\nabla\varphi|^2 - \frac{g\rho}{\Delta p}z + 2\frac{\sigma}{\Delta p}(\nabla\cdot\boldsymbol{n}) - \frac{p_0}{\Delta p}\left(\frac{V_0}{V}\right)^\lambda. \tag{23}$$

Now, use equations (21) and (22) into equation (23) we have,

$$\frac{d}{dt_*}\left(\frac{\varphi}{R_m}\sqrt{\frac{\rho}{\Delta p}}\right) = 1 + \frac{1}{2}\left|\nabla^*\left(\frac{\varphi}{R_m}\sqrt{\frac{\rho}{\Delta p}}\right)\right|^2 - \frac{g\rho R_m}{\Delta p}z_* + 2\frac{\sigma}{\Delta p R_m}(\nabla^*\cdot\boldsymbol{n}) - \frac{p_0}{\Delta p}\left(\frac{V_0}{V}\right)^\lambda. \tag{24}$$

Where,

$$\varphi_* = \frac{\varphi}{R_m}\sqrt{\frac{\rho}{\Delta p}}, \tag{25a}$$

$$t_* = \frac{t}{R_m}\sqrt{\frac{\Delta p}{\rho}}, \tag{25b}$$

$$\delta_* = \sqrt{\frac{\rho g R_m}{\Delta p}}, \tag{25c}$$

$$\sigma_* = \frac{\sigma}{R_m \Delta p}, \tag{25d}$$

$$\kappa_* = \nabla^*\cdot\boldsymbol{n}, \tag{25e}$$

$$\varepsilon = \frac{p_0}{\Delta p}. \tag{25f}$$

Thus, with assumptions given in equation (25), equation (24) becomes,

$$\frac{d\varphi_*}{dt_*} = 1 + \frac{1}{2}|\nabla^*\varphi_*|^2 - \delta^2_* z_* + 2\sigma_*\kappa_* - \varepsilon\left(\frac{V_0}{V}\right)^\lambda. \tag{26}$$

To normalize kinematic boundary condition (5), we start with,

$$\frac{d\boldsymbol{r}}{dt} = \frac{d\boldsymbol{r}}{dt_*}\cdot\frac{dt_*}{dt} = \frac{1}{R_m}\sqrt{\frac{\Delta p}{\rho}}\frac{d\boldsymbol{r}}{dt_*} = \sqrt{\frac{\Delta p}{\rho}}\frac{d\boldsymbol{r}_*}{dt_*}. \tag{27}$$

So, we have,

$$\frac{d\boldsymbol{r}_*}{dt_*} = \nabla^*\left(\frac{\varphi}{R_m}\sqrt{\frac{\Delta p}{\rho}}\right) = \nabla^*\varphi_*. \tag{28}$$

Finally, we have the complete dimensionless bubble dynamic model provided as follow:

Ahmed. H. *and*. Manmi .K . /ZJPAS: 2023, 35 (2): 63-77

68

$$c(\boldsymbol{p})\varphi(\boldsymbol{p}) = \int_S \left(\frac{\partial\varphi(\boldsymbol{q})}{\partial\boldsymbol{n}} G(\boldsymbol{p},\boldsymbol{q}) - \varphi(\boldsymbol{q}) \frac{\partial G(\boldsymbol{p},\boldsymbol{q})}{\partial\boldsymbol{n}} \right) dS(\boldsymbol{q}),$$

$$\frac{d\varphi_*}{dt_*} = 1 + \frac{1}{2}|\nabla^*\varphi_*|^2 - \delta^2_{\ *}z_* + 2\sigma_*\kappa_* - \varepsilon\left(\frac{V_0}{V}\right)^\lambda,$$

$$\frac{d\boldsymbol{r}_*}{dt_*} = \nabla\varphi_* \qquad \text{on bubble surface,}$$

$$\nabla\varphi_* \cdot \boldsymbol{n} = 0 \qquad \text{on rigid boundary ,}$$

(29)

with initial conditions,

$$\nabla\varphi_* = 0, \quad at \quad t_* = 0,$$
$$\varphi_* = 0, \quad at \quad t_* = 0.$$

5. Numerical Model

Assuming the flow to be axisymmetric, as is the case for a vertical bubble column perpendicular to an initially horizontal surface, θ_i can be arbitrarily taken as 0. So $\boldsymbol{p} = (r_i, 0, z_i)$ could be any point on the boundaries and $\boldsymbol{q} = (r, \theta, z)$ is the source point. The free space Green's funding we have (Lind and Phillips, 2010; Taib, 1985),

$$G(\boldsymbol{p},\boldsymbol{q}) = \frac{1}{\left((r+r_i)^2 + (z-z_i)^2 - 4rr_i\left(\cos(\theta/2)\right)^2 \right)^{1/2}},$$

(30)

and similarly,

$$\nabla\left(\frac{1}{|\boldsymbol{p}-\boldsymbol{q}|}\right) = -\frac{\left((r(\zeta)+r_i) - 2r_i\cos^2(\theta/2), (z(\zeta)-z_i) \right)}{\left((r+r_i)^2 + (z-z_i)^2 - 4rr_i\left(\cos(\theta/2)\right)^2 \right)^{3/2}}.$$

(31)

The surfaces S encasing each fluid region are parameterized with respect to (ζ, θ) as $\boldsymbol{q} = (r(\zeta), 0, z(\zeta))$. All derivatives with respect to θ are taken as zero due to the axisymmetric model. Equation (1) can be simplified into integrals over ζ. Consider first integrals of the form,

$$\int_S \frac{1}{|\boldsymbol{p}-\boldsymbol{q}|} dS(\boldsymbol{q}).$$

(32)

Hence the surface integral equation (32) becomes,

$$\int_S \frac{1}{|\boldsymbol{p}-\boldsymbol{q}|} dS(\boldsymbol{q}) = \int_0^1 \frac{4r(\zeta)\left[\left(\frac{dz(\zeta)}{d\zeta}\right)^2 + \left(\frac{dr(\zeta)}{d\zeta}\right)^2 \right]^{1/2}}{\left[(r(\zeta)+r_i)^2 + (z(\zeta)-z_i)^2 \right]^{1/2}} K(m)\, d\zeta.$$

(33)

Where, $\qquad m^2(\zeta) = \frac{4r(\zeta)r_i}{(r(\zeta)+r_i)^2 + (z(\zeta)-z_i)^2}$,

(34)

and where $K(m)$ is the complete elliptic integral of the first kind. Now consider the second integrals in equation (1) of the form,

$$\int_S \frac{\partial}{\partial\boldsymbol{n}}\left(\frac{1}{|\boldsymbol{p}-\boldsymbol{q}|}\right) dS(\boldsymbol{q}).$$

(35)

Hence we can write equation (35) as,

Ahmed. H. *and*. Manmi .K . /ZJPAS: 2023, 35 (2): 63-77

69

$$\int_S \frac{\partial G(\boldsymbol{p},\boldsymbol{q})}{\partial \boldsymbol{n}} dS(\boldsymbol{q})$$

$$= -4 \int_0^1 \frac{r(\zeta)}{\left[(r(\zeta)+r_i)^2 + (z(\zeta)-z_i)^2\right]^{3/2}} \left[\left(\frac{dz(\zeta)}{d\zeta}(r(\zeta)+r_i) - \frac{dr(\zeta)}{d\zeta}(z(\zeta)-z_i)\right.\right.$$

$$\left.\left. -\frac{2}{m^2(\zeta)}\frac{dz(\zeta)}{d\zeta}r_i\right)\frac{E(m)}{1-m^2(\zeta)} + \frac{2}{m^2(\zeta)}\frac{dz(\zeta)}{d\zeta}r_i K(m)\right]. \tag{36}$$

Where, $K(m)$ and $E(m)$ are the complete elliptic integrals of the first and second kind respectively. These integrals are approximated by,

$$K(m) = P(x) - Q(x)\ln x, \tag{37}$$
$$E(m) = R(x) - S(x)\ln x. \tag{38}$$
$$\text{Where,} \qquad x = 1 - m^2(\zeta), \tag{39}$$

and P, Q, R and S are tabulated polynomials (Curtiss, 2009; Taib, 1985).

The numerical model is based on the BIM, we need consider only half plane due to symmetricity. The bubble and rigid ellipsoid boundaries are discretized into n_b and n_r points as can been seen in Figure 1. Hence, The surface is replaced by a set of N linear segments S_j, with the potential and its normal derivative constant on each segment. The boundary integral equation is replaced by its collocation form using the midpoint of each linear segment,

$$2\pi\varphi_i + \sum_{j=1}^N \varphi_j \int_{S_j} \frac{\partial}{\partial \boldsymbol{n}}\left(\frac{1}{|\boldsymbol{p}_i - \boldsymbol{q}_j|}\right) dS(\boldsymbol{q}_j) = \sum_{j=1}^N \frac{\partial}{\partial \boldsymbol{n}}(\varphi_j) \int_{S_j}\left(\frac{1}{|\boldsymbol{p}_i - \boldsymbol{q}_j|}\right) dS(\boldsymbol{q}_j). \tag{40}$$

If we denoted $\frac{\partial \varphi_j}{\partial \boldsymbol{n}}$ by ψ_j, φ_j and ψ_j are assumed to be single valued at the end points of the linear segments which approximate the surface. If the segment is parameterized by ζ in the range $(0,1)$ we can define,

$$\left.\begin{array}{l} M_1(\zeta) = 1 - \zeta \\ M_2(\zeta) = \zeta \end{array}\right\}, \tag{41}$$

and use the isoperimetric approximations for both the surface and the functions. On segment S_j we have,

$$\left.\begin{array}{l} r(\zeta) = r_{j-1}M_1(\zeta) + r_j M_2(\zeta) \\ z(\zeta) = z_{j-1}M_1(\zeta) + z_j M_2(\zeta) \\ \varphi(\zeta) = \varphi_{j-1}M_1(\zeta) + \varphi_j M_2(\zeta) \\ \psi(\zeta) = \psi_{j-1}M_1(\zeta) + \psi_j M_2(\zeta) \end{array}\right\}. \tag{42}$$

The collocation points are moved to the end points of each segment, yielding $N+1$ equations in the $N+1$ unknowns. The integrals on each segment can be written,

$$\int_{S_j} \psi_j \left(\frac{1}{|\boldsymbol{p}_i - \boldsymbol{q}_j|}\right) dS(\boldsymbol{q}_j) = b_{1ij}\psi_{j-1} + b_{2ij}\psi_j, \tag{43}$$

where,

$$b_{kij} = 2\left(\frac{(z_j - z_{j-1})^2 + (r_j - r_{j-1})^2}{r_i}\right)^{1/2} \int_0^1 m\,K(m)\left(r_{j-1}(1-\zeta) + r_j(\zeta)\right)^{1/2} d\zeta. \tag{44}$$

$$\int_{S_j} \varphi_j \frac{\partial}{\partial \boldsymbol{n}}\left(\frac{1}{|\boldsymbol{p}_i - \boldsymbol{q}_j|}\right) dS(\boldsymbol{q}_j) = a_{1ij}\varphi_{j-1} + a_{2ij}\varphi_j, \tag{45}$$

where,

$$a_{kij} = \int_0^1 \left(\frac{1}{\left(\left(r_{j-1}(1-\zeta) + r_j(\zeta) + r_i\right)^2 + \left(z_{j-1}(1-\zeta) + z_j(\zeta) - z_i\right)^2\right)^{1/2}}\right.$$

Ahmed. H. *and*. Manmi .K . /ZJPAS: 2023, 35 (2): 63-77

70

$$\left[\frac{m^2}{r_i}\frac{E(m)}{1-m^2}\left((r_j-r_{j-1})(z_{j-1}(1-\zeta)+z_j(\zeta)-z_i)-(z_j-z_{j-1})(r_{j-1}(1-\zeta)+r_j(\zeta)+r_i)\right)\right.$$
$$\left.+\frac{E(m)}{1-m^2}\left(2(z_j-z_{j-1})\right)-2(z_j-z_{j-1})K(m)\right]d\zeta. \tag{46}$$

Therefore, in this model discretized from equation (1) with collocation points in the middle of each segment yields the following set of linear equations,

$$2\pi\varphi_i+\sum_{j=1}^{N}a_{ij}\,\varphi_j=\sum_{j=1}^{N}b_{ij}\,\psi_j. \tag{47}$$

We can write equation (40) in index form as,

$$2\pi\varphi_i+\sum_{j=1}^{N}\widehat{H}_{ij}\,\varphi_j=\sum_{j=1}^{N}G_{ij}\,\psi_j. \tag{48}$$

The terms of the matrices H and G in equation (48) are calculated numerically. Normally Gauss Legendre quadrature is used, unless the collocation point $\boldsymbol{p}_i$ is within the segment S_j, or is one of it endpoints, in which case the integrand is singular and must be treated specially. The singular integrals are calculated by subtracting the logarithmic term to remove the singularity. The integrals are approximated using a 6-point Gaussian quadrature rule. In this scheme the singular integral is transformed into two integrals, one integral contains no singularity which can be integrated by standard Gauss Legendre quadrature while the other integral contains an explicit logarithmic singularity. The integral containing the explicit logarithmic singularity can be integrated by a special quadrature scheme tabulated by (Stroud and Secrest, 1966.) for the integral,

$$\int_0^1 f(x)\ln\left(\frac{1}{x}\right)dx. \tag{49}$$

We can write equation (48) as,

$$c*\boldsymbol{\varphi}=\boldsymbol{G}\boldsymbol{\psi}-\boldsymbol{H}\boldsymbol{\varphi}. \tag{50}$$

Where $\boldsymbol{G}$ and $\boldsymbol{H}$ are the $N\times N$ influence coefficient matrices. It is noted that the diagonal elements of the influence coefficient matrices are integrated analytically and the non-diagonal elements are calculated numerically using six-point Gaussian quadrature. In case bubble in an infinite domain, the values of ψ on the bubble surface are unknown, while the values of φ are known, equation (50) can be re-writing as,

$$\boldsymbol{G}\boldsymbol{\psi}=(c\boldsymbol{I}+\boldsymbol{H})\boldsymbol{\varphi}, \tag{51}$$

where $\boldsymbol{I}$ is an $N\times N$ identity matrix. In case bubble near rigid boundary, the values of ψ on the bubble surface and the values of φ on the rigid surfaces are unknown, while the values of ψ on the rigid surfaces are equal to zero and the values of φ on the bubble surface are known, equation (50) can be re-writing as (Aziz, 2019; Mahmud, 2020; Aziz et al., 2019),

$$\begin{bmatrix}\boldsymbol{G}_{bb} & -\boldsymbol{G}_{br}\\ \boldsymbol{G}_{rb} & -\boldsymbol{G}_{rr}\end{bmatrix}\begin{bmatrix}\boldsymbol{\psi}_b\\ \boldsymbol{\varphi}_r\end{bmatrix}=\begin{bmatrix}-\boldsymbol{H}_{bb} & \boldsymbol{H}_{br}\\ -\boldsymbol{H}_{rb} & \boldsymbol{H}_{rr}\end{bmatrix}\begin{bmatrix}\boldsymbol{\varphi}_b\\ \boldsymbol{\psi}_r\end{bmatrix}. \tag{52}$$

Where the subscripts b and r are related to the nodes on the bubble surface and the boundary of the ellipsoid respectively. By solving the linear system in (52) we get ψ_b and φ_r. The tangtial velocity of the bubble surface can be obtained by using second order spline interpolation. Therefore, we can get velocity on the bubble surface by combining normal and tangential components. Then, the position of the bubble surface and the velocity potential on it at the next time step $t_*+\Delta t_*$ are obtained by time integration of equ-

Ahmed. H. *and*. Manmi .K . /ZJPAS: 2023, 35 (2): 63-77

71

ations (26) and (28) using fourth-order Runge-Kutta (RK4) scheme. A variable time-step size Δt_* is chosen as follows to save the central processing unit (CPU) time,

$$\Delta t_* = \frac{\Delta\varphi_*}{\max\left|1 + \frac{1}{2}|\nabla^*\varphi_*|^2 - \delta^2{}_* z_* + 2\sigma_*\kappa_* - \varepsilon\left(\frac{V_0}{V}\right)^\lambda\right|}, \tag{53}$$

Where $\Delta\varphi_*$ is a constant. The updated bubble surfaces were smoothed by using cubic spline (Curtiss, 2009; Shervani-Tabar, 1995).

6. Validations of the Numerical Model

The numerical model was compared with the RPE for a bubble in infinite fluid by considering different radiuses of the ellipsoid ($R_{c_*} = 200, 400, 600$). We considered that it was located at the center of the ellipsoid. In addition, self-validation has been performed by considering the model with and without the image method.

$$R_*\ddot{R}_* + \frac{3}{2}\left(\dot{R}_*\right)^2 = -1 - \frac{4\mu_*}{R_*}\dot{R}_* - \frac{2\sigma_*}{R_*}. \tag{54}$$

Where, R_* is radius of the bubble as a function of time, $\dot{R}_*$ is velocity,

$$\mu_* = \frac{4\mu}{R_m\sqrt{\rho\Delta p}}, \qquad \sigma_* = \frac{\sigma}{R_m\Delta p}. \tag{55}$$

RPE is the nonlinear second order differential equation that can not be solved analytically. However, it can be solved by using an efficient numerical approach such as fourth order Range-Kutta scheme (RK4). The characteristic parameters are chosen as $\varepsilon = 100$, $\gamma = 1.4$, $R_{*0} = 0.165$, $\sigma = 0$, $\Delta\varphi_* = 0.005$, $n_b = 61$ and $n_r = 91$ where, n_b and n_r are the number of nodes on the bubble surface and rigid wall boundaries respectively.

6.1 Comparison with RPE

In this section, the numerical results in the BIM for bubble oscillating inside rigid sphere with different non-dimensional radius ($R_{c_*} = 200, 400, 600$) compared with the numerical solution of the Rayleigh-Plesset equation (RPE) for a bubble at an infinite domain. The non-dimensionless equation can be express as (Castro, 2019; Brennen, 2014; Doherty, 2020; Aziz, 2019),

Figure 2 shows the bubble radius oscillations for at least three cycles for a bubble inside a rigid ellipsoid with different radius (200, solid green line), (400, dot dash blue line), (600, dash pink line) and (∞, dot black line) respectively as well as result of the RPE (solid red line). We can clearly observe that the numerical results approach to the result of the RPE when the ellipsoid radius increases.
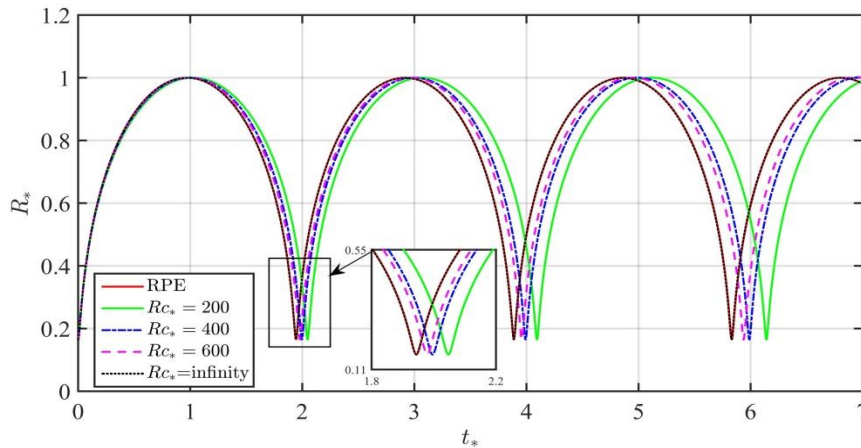
Figure 2: Comparison bubble radius with spherical wall radius. The parameters used for the cases are, $\Delta\varphi_* = 0.005$, $\varepsilon = 100$, $\gamma = 1.4, n_b = 61, n_w = 91$ and $\sigma = 0$.

Ahmed. H. *and*. Manmi .K . /ZJPAS: 2023, 35 (2): 63-77

72

6.2 Comparison with the Image Method

Suppose that a gas bubble oscillates near a rigid horizontal wall, as show in Figure (3), where the distance from center of the bubble to the rigid boundary denoted by h_r. In boundary integral equation (1), if we choose Green's function as follows (Shervani-Tabar, 1995; Lind, 2010; Walters and Phillips, 2016),

$$G(\boldsymbol{p}, \boldsymbol{q}) = \frac{1}{|\boldsymbol{p} - \boldsymbol{q}|} + \frac{1}{|\boldsymbol{p} - \boldsymbol{q}'|}, \qquad (56)$$

where, $\boldsymbol{q}'$ is the image of $\boldsymbol{q}$ on the rigid horizontal wall. The boundary of the

integral in equation (1) reduces only into S_b as $\frac{\partial G}{\partial \boldsymbol{n}}$ on the wall is zero. Therefore, the calculations (integrals) only on the bubble surface needed, eventually smaller liner system (52) need to be solved. However, finding such a Green's function like (56) for complex or non-straight boundary is challenging task. Therefore, direct method (without image, $G(\boldsymbol{p}, \boldsymbol{q}) = \frac{1}{|\boldsymbol{p}-\boldsymbol{q}|}$) can be used which usually more calculation is needed and eventually larger linear system must be solved.
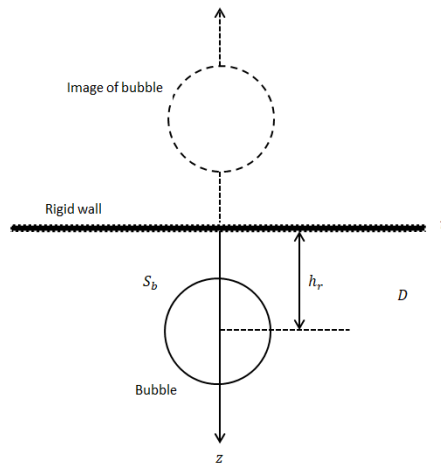
Figure 3: Schematic of a bubble motion near rigid wall using image method.

Here a typical case was considered to compare the results with and without image. We consider a bubble near rigid horizontal wall with $h_r = 1.5$. The characteristic parameters were $\varepsilon = 100$, $\gamma = 1.4$, $\sigma = 0$, $R_{*0} = 0.165$, $\Delta\varphi_* = 0.005$, $n_b = 81$ and $n_r = 202$. Where, n_b and n_r are the number of nodes on the bubble and rigid wall boundaries respectively. Figure 4 shows bubble shape at different instances obtained in the BIM with considering image method (dash red line) and

without image method (solid black line). The bubble expands spherically upon reach maximum volume. Slight flatten can be observed on the top side of the bubble surface due to blockage by the wall (see Figure 4a). The bubble shapes at all instances almost identical in both cases. However, there is slight delay (about 4%) in terms of time in without image method and this delay is developed with the time. It is clear that the bubble shapes are well agreed in both simulations in all instances.
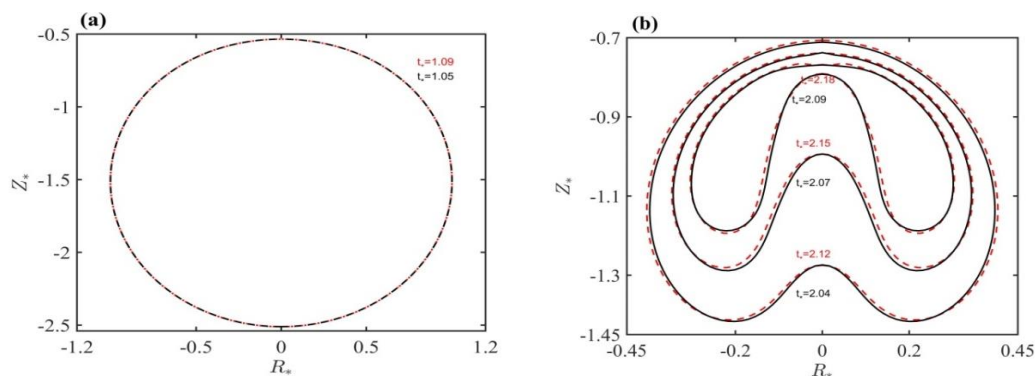
Figure 4: Bubble shape comparison in the BIM with considered image (dash red line) and without image (solid black line) at different instance. The parameters are chosen, $\varepsilon = 100$, $\gamma = 1.4$, $\sigma = 0$, $R_{*0} = 0.165$, $\Delta\varphi_* = 0.005$, $n_b = 81$ and $n_w = 202$.

Ahmed. H. *and*. Manmi .K . /ZJPAS: 2023, 35 (2): 63-77

73

7. Results and Discussions

In this section, bubble oscillations inside different shapes and sizes of spherical wall considered. In all considered cases in this section, the following parameters are kept fixed as: $\varepsilon = 100$, $\gamma = 1.4$, $\sigma = 0$, $R_{*0} = 0.165$, $\Delta\varphi_* = 0.005$, $n_b = 81$ and

$$I_* = \int_{S_*} \varphi_* \boldsymbol{n} dS_*,$$ (57)

and the centroid motion of the bubble along z-axis can be defined as,

$$C_z = \frac{\sum_{k=1}^{M} z_k A_k}{\sum_{k=1}^{M} A_k}.$$ (59)

Where the total number of the segments on the bubble surface is M, A_k is the area of the sector and k is the segment index on the bubble surface.

7.1 Bubble Inside a Rigid Sphere

Here, bubble dynamics inside rigid completely sphere ($R_{c_{*m}} = R_{c_{*M}} = 5$) has been investigated, when the center of the bubble initially shifted vertically by three different values ($h_{s*} = 1.2, 1.5, 2$) from the origin. Figure 5 shows the bubble surface shape at maximum volume (Figure 5a) and at the final stage of the first collapse phase (Figure 5b) for all three cases. Clearly, the bubble

$n_r = 405$. Where, n_b and n_r are the number of nodes on the bubble surface and rigid ellipsoid boundaries respectively. In all considered cases maximum jet velocity v_{jet*} at the collapse phase (which is velocity of bubble surface at node 1), Kelvin impulse I_*, which is defined as,

shapes remain spherical in the expansion phase (Figure 5a). In contrast, a high-speed liquid jet develops along the axis of symmetry toward the closest side of the sphere's surface at the end of the collapse phase (Figure 5b) in all considered h_{s*}. However, the jet width (shape) increases with h_{s*}. Further, the times at maximum value and jet impact have not changed significantly with h_{s*}.
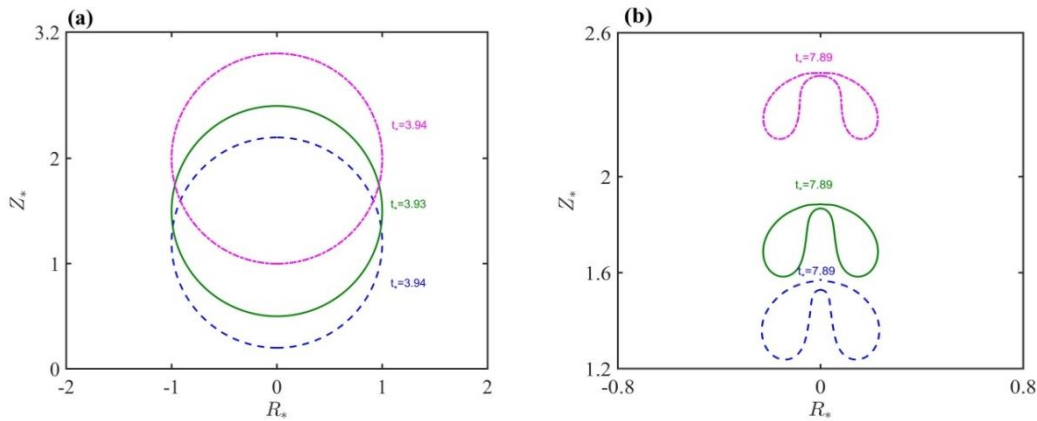
Figure 5: Bubble shapes at maximum volume and jet impact at the final stage of the collapse phase for different values of h_{s*} (blue dash line $h_{s*} = 1.2$), (green soiled line $h_{s*} = 1.5$), (magenta dot line $h_{s*} = 2$), parameters are used $\Delta\varphi_* = 0.005$, $\varepsilon = 100$, $\gamma = 1.4$, $R_{*0} = 0.165$, $n_b = 81$, $n_r = 405$ and $\sigma = 0$.

Table 1 provides jet velocity v_{jet*}, Kelvin impulse I_*, the centroid movement C_{z_*} versus h_{s*} for the considered cases in Figure 5 at the final step of the simulation. The jet velocity, centroid movement and Kelvin impulse are increase with h_{s*}. Jet velocity about (13% and 17%) increase when h_{s*} about (20% and 25%) increases. Therefore, jet velocity is linear proportional with h_{s*}.

Table 1 Provides jet velocity, Kelvin impulse and the centroid movement for the cases in Figure 5.

| h_{s*}	v_{jet*}	$|I_*|$	C_{z_*}
1.2	6.528929	0.022078	1.383338
1.5	7.489079	0.028394	1.716181
2	9.069419	0.041748	2.275916

7.2 Bubble Dynamics Inside a Rigid Ellipsoid

Here, we investigated a bubble collapse inside a rigid ellipsoid when the center of the bubble initially shifted vertically by three different values ($h_{s*} = 1.2, 1.5, 2$) from the origin. Two cases are considered. One is bubble dynamics inside a rigid ellipsoid with its major axis along a

Ahmed. H. *and*. Manmi .K . /ZJPAS: 2023, 35 (2): 63-77

74

horizontal line, while the second is that its major axis is along a vertical line. The major radius (R_{cM}) and minor radius (R_{cm}) of the ellipsoid are 10 and 5, respectively. All the other parameters are kept fixed as in Figure 5. Figures 6a and 6b illustrate the bubble shape at the maximum volume and jet impact at the final stage, respectively. Therefore, at the final stage of the first collapse phase, the jet width (shape) increases

with h_{s*}, the jet width is increased by (about 20% and 40%) when the bubble shifts by 1.5 and 2, respectively. Figures 6c and 6d show the numerical results at the maximum volume and jet impact when bubble dynamics inside a vertical ellipse. Because the jet is narrow, we can see different and the remaining parameters are the same as in Figures 6a and 6b.
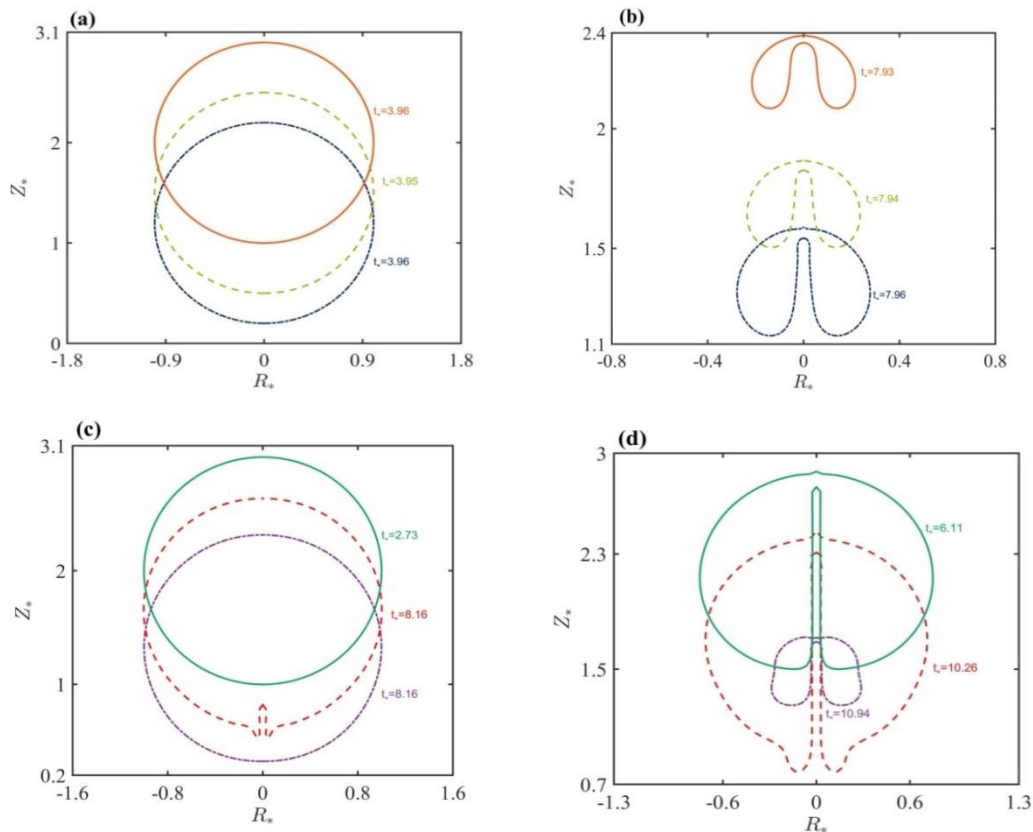
Figure 6: Bubble shapes at maximum volume and jet impact at final stage of the collapse phase for different value of h_{s*} (blue dash dot line $h_{s*} = 1.2$), (green dash line $h_{s*} = 1.5$) ,(orang soiled line $h_{s*} = 2$) for Figures a and b, and (red dash line $h_{s*} = 1.2$), (purple dash dot line $h_{s*} = 1.5$) ,(green soiled line $h_{s*} = 2$) for Figures c and d, other parameters are used $\Delta\varphi_* = 0.005$, $\varepsilon = 100$, $\gamma = 1.4, R_{*0} = 0.165$, $n_b = 81$, $n_r = 405$ and $\sigma = 0$.

Tables 2 and 3 provide jet velocity v_{jet*}, Kelvin impulse I_*, the centroid movement C_{z_*} versus h_{s*} for the considered cases in Figure 6 at the final step of the simulation. In Table 2 the jet velocity, Kelvin impulse and centroid movement are increase with h_{s*}. Jet velocity, Kelvin impulse and centroid movement about (23% and 6%), (24% and 34 %) and (20% and 25%) are increased respectively, when h_{s*} about (20% and 25%) increases. Therefore, in Table 3 the Kelvin impulse and centroid movement are increase with h_{s*}, while the jet velocity decreases when h_{s*} is increased. Kelvin impulse and centroid movement

approximately (10% and 6%) and (12% and 22%) increase respectively, when h_{s*} approximately (20% and 25%) increases. In both cases, the Kelvin impulse and centroid movement are increased, while the jet velocity is changed.

Table 2 Provides jet velocity, Kelvin impulse and the centroid movement for the cases in Figure 6b.

h_{s*}	v_{jet*}	$|I_*|$	C_{z_*}
1.2	4.693451	0.013913	1.338795
1.5	6.078141	0.018427	1.665488
2	6.479898	0.027984	2.217930

Ahmed. H. *and*. Manmi .K . /ZJPAS: 2023, 35 (2): 63-77

75

Table 3 Provides jet velocity, Kelvin impulse and the centroid movement for the cases in Figure 6d.

h_{s*}	v_{jet*}	$|I_*|$	C_{z*}
1.2	6.094188	0.019452	1.464482
1.5	2.314295	0.021658	1.670291
2	0.806709	0.022980	2.152943

8. Summary and Conclusions

The dynamics of a gas bubble inside a rigid sphere and rigid ellipsoid have been investigated numerically using the boundary integral method in axisymmetric configuration. The numerical model was validated by RPE and self-validated with considering image and without image for choosing Green's function in the BIM. In all numerical results, the initial bubble center shifted to the top along the axis of symmetry by (h_{s*}=1.2, 1.5 and 2) for three different shapes of boundaries, which are completely sphere ($R_{c*m} = R_{c*M} = 5$), ellipsoid with major axis along horizontal line (R_{cM} major radius, R_{cm} minor radius) and ellipsoid with major axis along vertical line (R_{cM} major radius, R_{cm} minor radius) respectively. In all considered cases, we noticed that velocity and width of the jet at final stage, magnitude kelvin impulse and centroid movement increases proportionally with h_{s*}. However, when the bubble collapse inside ellipsoid with major axis along vertical line jet velocity decreases with h_{s*}.

References:

Aziz, I.A, 2019, *Modelling Three Dimensional Bubble Dynamics Near Rigid Boundaries Using Boundary Integral Method* (Doctoral dissertation, College of Science, Salahaddin University-Erbil).

Aziz, I.A., Manmi, K.M., Saeed, R.K. and Dadvand, A., 2019. Modeling three dimensional gas bubble dynamics between two curved rigid plates using boundary integral method. *Engineering Analysis with Boundary Elements*, *109*, pp.19-31.

Alehossein, H. and Qin, Z., 2007. Numerical analysis of Rayleigh–Plesset equation for cavitating water jets. *International Journal for Numerical Methods in Engineering*, *72*(7), pp.780-807.

Batchelor, G.K., 2000. *An introduction to fluid dynamics*. Cambridge university press.

Brennen, C.E., 2014. *Cavitation and bubble dynamics*. Cambridge university press.

Blake, J.R., Taib, B.B. and Doherty, G., 1986. Transient cavities near boundaries. Part 1. Rigid boundary. *Journal of Fluid Mechanics*, *170*, pp.479-497.

Blake, J.R., Taib, B.B. and Doherty, G., 1987. Transient cavities near boundaries Part 2. Free surface. *Journal of Fluid Mechanics*, *181*, pp.197-212.

Brujan, E.A., Noda, T., Ishigami, A., Ogasawara, T. and Takahira, H., 2018. Dynamics of laser-induced cavitation bubbles near two perpendicular rigid walls. *Journal of Fluid Mechanics*, *841*, pp.28-49.

Castro, A. M. B., 2019. *Lagrangian tracking of the cavitation bubble*. Faculty of machining engineering, Brno university of technology.

Cengel, Y.A., Cimbala, J.M., 2014. Fluied mechanics fundamentals and applications.

Cochard, H., 2006. Cavitation in trees. *Comptes Rendus Physique*, *7*(9-10), pp.1018-1026.

Cui, J., Zhou, T.R., Huang, X. and Li, Z.C., 2021. Experimental study of bubble dynamics in the neighbourhood of a vertical incomplete boundary. *Ultrasonics Sonochemistry*, *75*, p.105587.

Cui, J., Li, M.Y., Sun, S.Y., Xu, W., Zhou, T.R. and Zhang, X., 2022. Experimental studies of bubble dynamics under a broken horizontal plate. *Ocean Engineering*, *245*, p.110459.

Curtiss, G.A., 2009. *Non-linear, non-spherical bubble dynamics near a two fluid interface* (Doctoral dissertation, University of Birmingham).

Chahine, G.L. and Perdue, T.O., 1990, January. Simulation of the three-dimensional behavior of an unsteady large bubble near a structure. In *AIP Conference Proceedings* (Vol. 197, No. 1, pp. 188-199). American Institute of Physics.

Doherty, W., 2019. The Influence of a Magnetic Field on the Dynamics of Spherical Bubbles in Viscoelastic Fluids.

Doherty, W., 2020. Dynamics of Cavitation Bubbles in Viscoelastic Fluids.

Dawoodian, M., Dadvand, A. and Nematollahi, A., 2015. Simulation of bubble dynamics near a plate with an aperture in a vertical cylinder using a combined boundary element-finite difference method. *Engineering Analysis with Boundary Elements*, *59*, pp.187-197.

Doinikov, A.A. and Marmottant, P., 2018. Natural oscillations of a gas bubble in a liquid-filled cavity located in a viscoelastic medium. *Journal of Sound and Vibration*, *420*, pp.61-72.

Doinikov, A.A., Dollet, B. and Marmottant, P., 2018. Model for the growth and the oscillation of a cavitation bubble in a spherical liquid-filled cavity enclosed in an elastic medium. *Physical Review E*, *97*(1), p.013108.

Doinikov, A.A., Bienaimé, D., Gonzalez-Avila, S.R., Ohl, C.D. and Marmottant, P., 2019. Nonlinear dynamics of two coupled bubbles oscillating inside a liquid-filled cavity surrounded by an elastic medium. *Physical Review E*, *99*(5), p.053106.

Fourar, M. and Bories, S., 1995. Experimental study of air-water two-phase flow through a fracture (narrow channel). *International journal of multiphase flow*, *21*(4), pp.621-637.

Franc, J.P. and Michel, J.M., 2006. *Fundamentals of cavitation* (Vol. 76). Springer science & Business media.

Jensen, K.H., Berg-Sørensen, K., Bruus, H., Holbrook, N.M., Liesche, J., Schulz, A., Zwieniecki, M.A. and Bohr, T., 2016. Sap flow and sugar transport in plants. *Reviews of modern physics*, *88*(3), p.035007.

Ahmed. H. *and*. Manmi .K . /ZJPAS: 2023, 35 (2): 63-77

76

Keller, J.B. and Miksis, M., 1980. Bubble oscillations of large amplitude. *The Journal of the Acoustical Society of America*, *68*(2), pp.628-633.

Keller, J.B. and Kolodner, I.I., 1956. Damping of underwater explosion bubble oscillations. *Journal of applied physics*, *27*(10), pp.1152-1161.

Klaseboer, E. and Khoo, B.C., 2006. A modified Rayleigh–Plesset model for a non-spherically symmetric oscillating bubble with applications to boundary integral methods. *Engineering analysis with boundary elements*, *30*(1), pp.59-71.

Klaseboer, E., Fernandez, C.R. and Khoo, B.C., 2009. A note on true desingularisation of boundary integral methods for three-dimensional potential problems. *Engineering analysis with boundary elements*, *33*(6), pp.796-801.

Lauterborn, W. and Kurz, T., 2010. Physics of bubble oscillations. *Reports on progress in physics*, *73*(10), p.106501.

Lindau, O. and Lauterborn, W., 2003. Cinematographic observation of the collapse and rebound of a laser-produced cavitation bubble near a wall. *Journal of Fluid Mechanics*, *479*, pp.327-348.

Leighton, T.G., 2007. Derivation of the Rayleigh-Plesset equation in terms of volume.

Lin, H., Storey, B.D. and Szeri, A.J., 2002. Inertially driven inhomogeneities in violently collapsing bubbles: the validity of the Rayleigh–Plesset equation. *Journal of Fluid mechanics*, *452*, pp.145-162.

Lind, S.J., 2010. *Numerical study of the effect of viscoelasticity on cavitation and bubble dynamics*. Cardiff University (United Kingdom).

Lind, S.J. and Phillips, T.N., 2010. Spherical bubble collapse in viscoelastic fluids. *Journal of non-Newtonian fluid mechanics*, *165*(1-2), pp.56-64.

Li, Z., Sun, L., Zong, Z. and Dong, J., 2012. Some dynamical characteristics of a non-spherical bubble in proximity to a free surface. *Acta Mechanica*, *223*(11), pp.2331-2355.

Li, Z., Sun, L. and Zong, Z., 2013. Numerical analysis of gas bubbles in close proximity to a movable or deformable body. *Archive of Applied Mechanics*, *83*(12), pp.1715-1737.

Liu, W., 2018. *Bubble dynamics in a compressible viscous liquid* (Doctoral dissertation, University of Birmingham).

Liu, B., Cai, J. and Huai, X., 2014. Heat transfer with the growth and collapse of cavitation bubble between two parallel heated walls. *International Journal of Heat and Mass Transfer*, *78*, pp.830-838.

Manmi, K., 2015. *Three dimensional acoustic microbubble dynamics near rigid boundary* (Doctoral dissertation, University of Birmingham).

Mahmud, M.H., 2020. *Microbubble dynamics near rigid boundaries* (Doctoral dissertation, University of Birmingham).

Mehran, S., Rouhi, S., Rouzbahani, F. and Haghgoo, E., 2010. Dynamics of a Vapour Bubble inside a Vertical Rigid Cylinder in the Absence of Buoyancy Forces.World Acad. Sci., Eng. Technol, 63, pp.278-283.

Marti, D., Krüger, Y., Fleitmann, D., Frenz, M. and Rička, J., 2012. The effect of surface tension on liquid–gas equilibria in isochoric systems and its application to fluid inclusions. *Fluid phase equilibria*, *314*, pp.13-21.

Nadir, N.N. and MANMI, K.M.A., 2020. Comparative Investigation of the Spherical Acoustic Microbubble Models in an Unbounded Liquid. *Zanco Journal of Pure and Applied Sciences*, *32*(4), pp.82-88.

Ni, B.Y., Zhang, A., Wang, Q.X. and Wang, B., 2012. Experimental and numerical study on the growth and collapse of a bubble in a narrow tube. *Acta Mechanica Sinica*, *28*(5), pp.1248-1260.

Ogasawara, T., Tsubota, N., Seki, H., Shigaki, Y. and Takahira, H., 2015, November. Experimental and numerical investigations of the bubble collapse at the center between rigid walls. In *Journal of Physics: Conference Series* (Vol. 656, No. 1, p. 012031). IOP Publishing.

Plesset, M.S. and Prosperetti, A., 1977. Bubble dynamics and cavitation. *Annual review of fluid mechanics*, *9*(1), pp.145-185.

Plesset, M.S., 1954. On the stability of fluid flows with spherical symmetry. *Journal of Applied Physics*, *25*(1), pp.96-98.

Rafizadeh, S. and Dadvand, A., 2020. Droplet generation via oscillation of a transient bubble inside a funnel-like chamber. *Engineering Analysis with Boundary Elements*, *113*, pp.416-427.

Rayleigh, L., 1917. VIII. On the pressure developed in a liquid during the collapse of a spherical cavity. *The London, Edinburgh, and Dublin Philosophical Magazine and Journal of Science*, *34*(200), pp.94-98.

Sarkar, P., 2019. *Simulation of cavitation erosion by a coupled CFD-FEM approach* (Doctoral dissertation, Université Grenoble Alpes).

Shervani-Tabar, M.T., 1995. Computer study of a cavity bubble near a rigid boundary, a free surface, and a compliant wall.

Soliman, W., Nakano, T., Takada, N. and Sasaki, K., 2010. Modification of Rayleigh–Plesset theory for reproducing dynamics of cavitation bubbles in liquid-phase laser ablation. *Japanese Journal of Applied Physics*, *49*(11R), p.116202.

Stroud, A.H. and Secrest, D., 1966. *Gaussian Quadrature Formulas: By AH Stroud and Don Secrest*. Prentice-Hall.

Su, B., Yao, X. and Cui, X., 2022. Experimental research of underwater explosion bubble dynamics between two parallel plates with various distances. *Applied Ocean Research*, *122*, p.103081.

Taib, B.B., 1985. Boundary integral method applied to cavitation bubble dynamics.

Tey, W.Y., Alehossein, H., Qin, Z., Lee, K.M., Kang, H.S. and Lee, K.Q., 2020, March. On stability of time marching in numerical solutions of rayleigh-plesset equation for ultrasonic cavitation. In *IOP Conference Series: Earth and Environmental Science* (Vol. 463, No. 1, p. 012117). IOP Publishing.

Ahmed. H. *and*. Manmi .K . /ZJPAS: 2023, 35 (2): 63-77

77

Vincent, O., Sessoms, D.A., Huber, E.J., Guioth, J. and Stroock, A.D., 2014. Drying by cavitation and poroelastic relaxations in extreme ink-bottle porous media. *Phys. Rev. Lett.*, *113*, p.134501.

Walters, M.J. and Phillips, T.N., 2016. A non-singular boundary element method for modelling bubble dynamics in viscoelastic fluids. *Journal of Non-Newtonian Fluid Mechanics*, *235*, pp.109-124.

Wang, Q.X. and Manmi, K., 2014. Three dimensional microbubble dynamics near a wall subject to high intensity ultrasound. *Physics of Fluids*, *26*(3), p.032104.

Wang, Q.X., 2013. Non-spherical bubble dynamics of underwater explosions in a compressible fluid. *Physics of Fluids*, *25*(7), p.072104.

Wang, Q.X., 2017. Oscillation of a bubble in a liquid confined in an elastic solid. *Physics of Fluids*, *29*(7), p.072101.

Wang, S.P., Wang, Q.X., Leppinen, D.M., Zhang, A.M. and Liu, Y.L., 2018. Acoustic bubble dynamics in a microvessel surrounded by elastic material. *Physics of Fluids*, *30*(1), p.012104.

Zhang, X., Li, F., Wang, C., Guo, J., Mo, R., Hu, J., Chen, S., He, J. and Liu, H., 2022. Radial oscillation and translational motion of a gas bubble in a micro-cavity. *Ultrasonics Sonochemistry*, *84*, p.105957.

Zhang, A.M., Cui, P. and Wang, Y., 2013. Experiments on bubble dynamics between a free surface and a rigid wall. *Experiments in fluids*, *54*(10), pp.1-18.